

Supplemental Material to “New Angles on Energy Correlators”

Samuel Alipour-fard,^{1,*} Ankita Budhraj,^{2,†} Jesse Thaler,^{1,‡} and Wouter J. Waalewijn^{2,3,§}

¹*Center for Theoretical Physics, Massachusetts Institute of Technology, Cambridge, MA 02139, USA*

²*Nikhef, Theory Group, Science Park 105, 1098 XG, Amsterdam, The Netherlands*

³*Institute for Theoretical Physics Amsterdam and Delta Institute for Theoretical Physics, University of Amsterdam, Science Park 904, 1098 XH Amsterdam, The Netherlands*

In this *Supplemental Material*, we provide additional details regarding the parametrization we introduce for projected and resolved N -point energy correlators (PENCs and RENCs, respectively). In App. A, we discuss and visualize the theoretical similarities between our new parametrization and the standard parametrization for PENCs. In App. B, we discuss the algorithmic implementation and the performance of our new parametrization. We also show additional results using Open Data, up to RE4Cs, in App. C, and visualize the process dependence of our PENCs and RENCs on samples for QCD-, W -, and top-initiated jets in App. D. Finally, in App. E, we discuss the qualitative behavior of non-perturbative effects.

Appendix A: NLL Equivalence to Traditional PENCs

We first emphasize that the parametrization we propose for PENCs only differs from the traditional PENCs studied in the literature through the jet function. In particular, the factorization for our new parametrization is identical to that of the traditional PENCs in the collinear limit [1, 2]:

$$\Sigma_N(R_1, Q) = \int_0^1 dx x^N \sum_i H_i\left(x, \frac{Q}{\mu}\right) \cdot J_i\left(\frac{x^2 Q^2 R_1^2}{\mu^2}\right), \quad (\text{A1})$$

where the flavor index $i = q, g$ is summed over. At a specific perturbative order, the expressions also depend on μ through $\alpha_s(\mu)$. Eq. (A1) states that the resummed cross section for the PENCs is governed by:

- A *hard function* $H_i(x, Q/\mu)$, characterizing the number density of partons of partonic flavor i (e.g. up quark, gluon) emerging from the hard process at a given momentum fraction x . The hard function is dependent on a renormalization scale μ . Notably, the hard function is independent of the parametrization used for the PENC.
- A *jet function* $J_i(x^2 Q^2 R_1^2/\mu^2)$, describing the subsequent evolution of the energetic parton i into a jet of “final-state” partons on which the PENC is then measured. Unlike the hard function, the jet function depends on the parametrization of the observable.

In this appendix, we quantify the difference between the jet function for our new PENC (the R_1 jet function) and the traditional PENC (the R_L jet function). Using theoretical arguments and numerical evidence, we argue that their difference is only relevant at next-to-next-to-leading-logarithmic (NNLL) order.

The resummation of logarithms of R_1 in Σ_N can be achieved by evaluating the hard function at the scale $\mu_H \sim Q$ and the jet function at the scale $\mu_J \sim QR_1$, and using the renormalization group equations to evolve them to a common scale μ . Since the full PENC is independent of μ , and the hard function is independent of the specific parametrization of the PENC, the renormalization group evolution for the jet function is also parametrization-independent (even if its functional form is not).

Within a jet consisting of two outgoing particles, the PENC we introduce and the traditional PENC are exactly the same, since $R_1 = R_L$. Therefore, the R_1 jet function the R_L jet function are identical at $\mathcal{O}(\alpha_s)$, implying that the cross section for the new and traditional PENC will be equal at NLL, as these are single-logarithmic observables. However, R_1 and R_L will differ for a jet of three particles or more, corresponding to an $\mathcal{O}(\alpha_s^2)$ difference between the R_1 and R_L jet functions, and an NNLL effect in the resummed cross section.

Though R_1 and R_L differ in a generic jet, we note that $R_1 \leq R_L \leq 2R_1$ by the triangle inequality. Therefore, we expect an approximate relationship between the two of the form $R_L \sim (1 + c)R_1$ with $0 < c < 1$. Furthermore, NLL

* samuelaf@mit.edu

† abudhraj@nikhef.nl

‡ jthaler@mit.edu

§ w.j.waalewijn@uva.nl

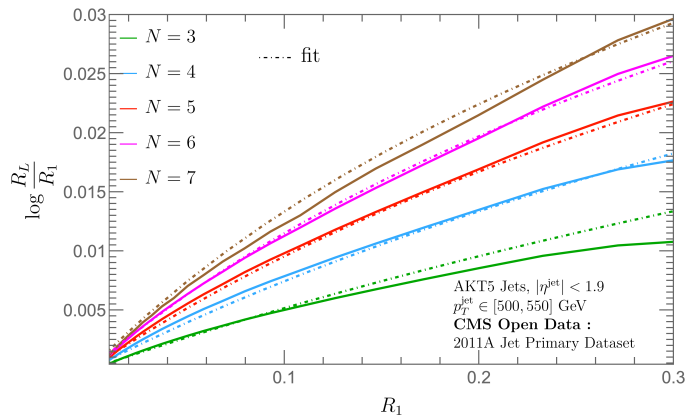


FIG. 1. Difference between the new parametrization (R_1) and the old parametrization (R_L) obtained from corresponding quantiles of the cumulative distributions. The dashed lines correspond to a fit (of the overall coefficient) of the difference $\log(R_L/R_1)$ to $\frac{\alpha_s}{\pi} \log(1 + R_L(N-1))$ for integer values of N from 3 to 7.

equivalence of the R_1 and R_L jet functions implies that $c \sim \mathcal{O}(\alpha_s)$. In particular, writing the N^k LL contribution to the traditional PENC as $\sum_n d_{n,k} \alpha_s^{n+k} \log^n R_L$ and inserting $R_L = (1+c)R_1$ yields:

$$\begin{aligned} \sum_{n,k} d_{n,k} \alpha_s^{n+k} \log^n [R_1(1+c)] &= \sum_{n,k} d_{n,k} \alpha_s^{n+k} [\log R_1 + \log(1+c)]^n \\ &= \sum_{m,k,k'} \binom{m+k'}{m} d_{m+k',k'} \alpha_s^{m+k+k'} \log^m R_1 \log^{k'}(1+c), \end{aligned} \quad (\text{A2})$$

where in the final line we have written $n = m + k'$. The terms with $k' = 0$ give precisely the traditional PENC but with the argument R_L replaced by R_1 . For $k' = 1$ this would represent an NLL effect. However, the difference between our new PENC and the traditional PENC starts at NNLL, implying that $\log(1+c) \sim \mathcal{O}(\alpha_s)$ and thus $c \sim \mathcal{O}(\alpha_s)$.

Finally, we present additional numerical evidence that $R_L \sim (1+c)R_1$ with $c \sim \mathcal{O}(\alpha_s)$ by using the cumulative distributions for R_1 and R_L to construct a correspondence between R_1 and R_L using quantiles [3]. In particular, we numerically invert the equation

$$\Sigma_N^{\text{new}}(R_1) = \Sigma_N^{\text{old}}(R_L(R_1)), \quad (\text{A3})$$

to find a functional form for $R_L(R_1)$. In words, Eq. (A3) selects a function $R_L(R_1)$ for which our new PENC and the traditional PENC have equivalent cumulative distributions. Fig. 1 displays the difference between $\log(R_L(R_1))$ and $\log R_1$, as a function of R_1 , for $N = 3, 4, 5, 6$, and 7 . The dashed lines correspond to a fit (of the overall constant) to the form $c \sim \alpha_s/\pi \log[1 + (N-1)R_L]$. This provides numerical evidence for our theoretical arguments that the R_1 and R_L jet functions are equivalent at NLL, and that $R_L = [1 + \mathcal{O}(\alpha_s)]R_1$.

Appendix B: Samples, Implementation, and Performance

The studies of this Letter involve both CMS Open Data jet samples from the CMS 2011A Jet Primary Dataset [4, 5] – also available in MIT Open Data format [6, 7] – and jets in simulated proton-proton collision events generated using `Pythia 8.310` [8] with the default Monash tune [9]. In `Pythia 8.310`, we consider jets initiated by QCD interactions, W bosons, and top quarks, and generate events at hadron level including initial-state radiation, final-state radiation, and multiparton interactions.

Both the CMS 2011A dataset and our simulated `Pythia` events feature anti- k_t jets [10] with transverse momenta $p_{T,\text{jet}} \in [500, 550]$ GeV and pseudo-rapidity $|\eta^{\text{jet}}| < 1.9$; however, the CMS dataset involves jets of radius $R_{\text{jet}} = 0.5$, while our `Pythia` studies use jets of radius $R_{\text{jet}} = 0.8$, which are more appropriate for capturing the substructure of boosted W -boson- and top-quark-initiated jets. Our samples are summarized in Table I. Finally, we note that all of the traditional PENCs shown in this work are calculated with the `EnergyEnergyCorrelators` package [11].

Jet Sample	Center of Mass Energy	AK Radius	
CMS Open Data	7 TeV	$R = 0.5$	
Pythia 8.310			Command in Pythia
QCD Jets	14 TeV	$R = 0.8$	HardQCD:all=on
W Jets	14 TeV	$R = 0.8$	WeakDoubleBoson:ffbar2WW=on
Top Jets	14 TeV	$R = 0.8$	Top:gg2ttbar=on, Top:qqbar2ttbar=on

TABLE I. Jet samples used in this work. All jets have transverse momenta $p_{T,\text{jet}} \in [500, 550]$ GeV and pseudo-rapidity $|\eta^{\text{jet}}| < 1.9$. The color of each row corresponds to the color in the plots of the associated jet sample.

ALG I. Pseudocode for PENC(R_1)

```

1: Output: Normalized 1-dimensional histogram
2:   containing the PENC
3:
4: Initialize 1D histogram to contain the PENC
5: # Loop over jets in a sample:
6: for all  $i$  from 1 to  $n_{\text{jets}}$  do
7:    $jet \leftarrow$  a jet from the desired sample
8:   # Loop over choices for particle  $s$  in the jet:
9:   for all particles  $s$  in  $jet$  do
10:    # Calculate energy weight
11:     $z_s \leftarrow p_{T,s}/(\sum_j p_{T,j})$ 
12:    Sort particles in  $jet$  by angle to  $s$ ,
13:    from smallest to largest
14:    # Prepare to record total weight within a
15:    # distance  $R_1$  of  $s$ , beginning with  $R_1 = 0$ 
16:    Initialize  $sum_{z_1} \leftarrow z_s$ 
17:     $histogram[0] += z_s^N$ 
18:    # Loop over remaining particles  $i_1$ 
19:    for all  $i_1$  from 1 to  $\text{len}(\text{particles})$  do
20:       $R_1 \leftarrow$  angle between  $s$  and  $\text{particle}[i_1]$ 
21:       $z_1 \leftarrow p_{T,i_1}/(\sum_j p_{T,j})$ 
22:      # Calculate contribution to  $d\Sigma$ , and
23:      # update hist. bin for  $R_1$ 
24:       $histogram[R_1] += z_s \times$ 
25:       $((sum_{z_1} + z_1)^{N-1} - sum_{z_1}^{N-1})$ 
26:      # Update sum on weights within  $R_1$ 
27:       $sum_{z_1} += z_1$ 
28:    end for
29:  end for
30: end for
31:
32: # histogram currently contains  $d\Sigma$ , and we want
33: #  $\text{PENC} = d\Sigma/dR_1$ 
34: Process histogram into a probability density by
35:   normalizing it relative to bin widths
36: Write histogram to output file

```

ALG II. Pseudocode for RE3C(R_1, R_2, ϕ_2)

```

1: Output: Normalized 3-dimensional histogram
2:   containing the RE3C
3:
4: Initialize 3D histogram to contain the RE3C
5: # Loop over jets in a sample:
6: for all  $i$  from 1 to  $n_{\text{jets}}$  do
7:    $jet \leftarrow$  a jet from the desired sample
8:   # Loop over choices for particle  $s$  in the jet:
9:   for all particles  $s$  in  $jet$  do
10:    # Calculate energy weight
11:     $z_s \leftarrow p_{T,s}/(\sum_j p_{T,j})$ 
12:    Sort particles in  $jet$  by angle to  $s$ ,
13:    from smallest to largest
14:    # Loop over remaining particles  $i_1$  and  $i_2$ ,
15:    for all  $i_1$  from 1 to  $\text{length}(\text{particles})$  do
16:       $R_1 \leftarrow$  angle between  $s$  and  $\text{particle}[i_1]$ 
17:       $z_1 \leftarrow p_{T,i_1}/(\sum_j p_{T,j})$ 
18:      # where  $i_2$  is closer to  $s$  than  $i_1$ 
19:      for all  $i_2 < i_1$  do
20:         $R_2 \leftarrow$  angle between  $s$  and  $i_2$ 
21:         $z_2 \leftarrow p_{T,i_2}/(\sum_j p_{T,j})$ 
22:         $\phi_2 \leftarrow$  angle associated with  $i_1$ - $s$ - $i_2$ 
23:        # Calculate contribution to  $d\Sigma$ ,
24:        # and update associated hist. bin
25:         $histogram[R_1][R_2][\phi_2] += z_s \cdot z_1 \cdot z_2$ 
26:      end for
27:    end for
28:  end for
29: end for
30:
31: # histogram currently contains  $d\Sigma$ , and we want
32: #  $\text{RE3C} = d\Sigma/dR_1 dR_2 d\phi_2$ 
33: Process histogram into a probability density by
34:   normalizing it relative to bin widths
35: Write histogram to output file

```

We also provide pseudocode of our new algorithms for calculating PENCs and RE3Cs in Algs. I and II, respectively. Alg. I exemplifies how the parametrization we introduce for the PENC (i.e. of angles with respect to a specific particle s) simplifies the N -dependence of our new PENC, dramatically speeding up the associated computation. In particular, the algorithm has identical runtime behavior for any value of N , and *there are no additional computational complications for large or non-integer N* . For completeness, we also present pseudocode for the RE3C in Alg. II, which features similar computational simplicity and can be easily generalized to a double-projected ENC as discussed in the main text. For a more complete and technical description of each computation, including contributions in

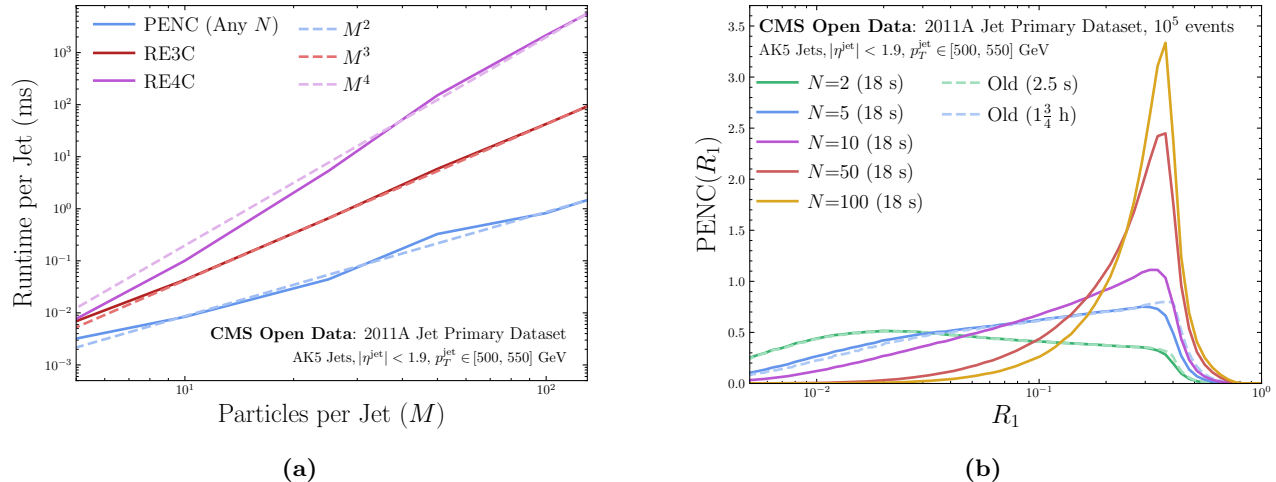


FIG. 2. Plots emphasizing the computational performance of the energy correlators we introduce in this work. **(a)** Runtime of the PENC and RENC code of Ref. [12] on CMS Open Data as a function of the number of particles in a jet, together with a polynomial fit to guide the eye. **(b)** PENCs for $N = 2, 5, 10, 50$, and 100 , each computed using on 10^5 CMS Open Data jets in less than thirty seconds. The solid lines show the PENCs introduced in this work, and the dashed lines show the traditional PENCs. Even for $N = 5$, the traditional computation takes 6266 seconds (close to 2 hours) to run on the same CMS Open Data samples, and the computation time grows exponentially as N increases. The large values of N , which are computationally inaccessible to the traditional PENC even for $N = 10$, are chosen to stress that the PENCs we introduce in this work make quick work of previously unimaginable computations.

which the same particle enters multiple times in the correlator (often called contact terms), please consult our full implementation on GitHub at [ResolvedEnergyCorrelators](#) [12].

Finally, in Fig. 2, we display the computational runtime of our code for the evaluation of PENCs and RENCs on jet samples from CMS Open Data. Fig. 2(a) shows how the scaling time for each nearly follows an M^r scaling, where r indicates the number of resolved emissions. Furthermore, the independence of the runtime on the value of N allows us to compute the PENC for enormous, and previously unimaginable, values of N ; some examples up to $N = 100$ are shown in Fig. 2(b). We highlight that our implementation takes similar runtime for all values of N . Therefore, we expect the PENC we introduce in this work to significantly benefit ongoing studies which apply energy correlators in jets produced in heavy-ion collisions for revealing the emergent scales of the quark-gluon plasma in these environments.

Appendix C: Visualizing CMS Open Data with Resolved Correlators

In this appendix, we provide additional polar heat maps, or *bullseye* visualizations, of RE3Cs and RE4Cs evaluated on CMS Open Data, which yield an intuitive view into the internal structure of jets enabled by our new parametrization. We expect that similar visualizations will benefit current and future studies of jet substructure at the LHC.

The bullseyes for the RE3C, shown in Fig. 3, have a radial variable corresponding to the ratio $R_2/R_1 < 1$, with a polar angle corresponding to ϕ_2 . Similarly, the bullseyes for the RE4C in Fig. 4 use the radial variable $R_3/R_2 < 1$ and the corresponding polar variable ϕ_3 . The bullseyes are normalized to a radial measure, such that the bullseye plots provide a faithful representation of each correlator; for the RE3C, the bullseye is normalized to unity against the measure $d \log R_1 \times R_2 dR_2 d\phi_2$, while the bullseyes for the RE4C are normalized to unity against $d \log R_1 d(R_2/R_1) d\phi_2 \times R_3 dR_3 d\phi_3$.

RE3Cs are shown in Fig. 3 for several R_1 bins, and RE4Cs are shown in Fig. 4 for several R_1 and ϕ_2 bins with a fixed R_2/R_1 bin. We note that the RE3C distributions are quite similar across different R_1 bins. On the other hand, for R_2 near R_1 , the RE4C distributions exhibit distinct patterns of radiation depending on the value of ϕ_2 . In particular, Fig. 4 prominently visualizes the collinearly enhanced correlations in the RE4C when ϕ_3 is near $-\phi_2$ and R_3 is near R_1 , i.e. when particle i_3 approaches particle i_1 . For small R_2 , these correlations diminish, and the bullseye visualizations for the RE4C look very similar to that of the RE3C, reflecting the near-scale-invariance of QCD.

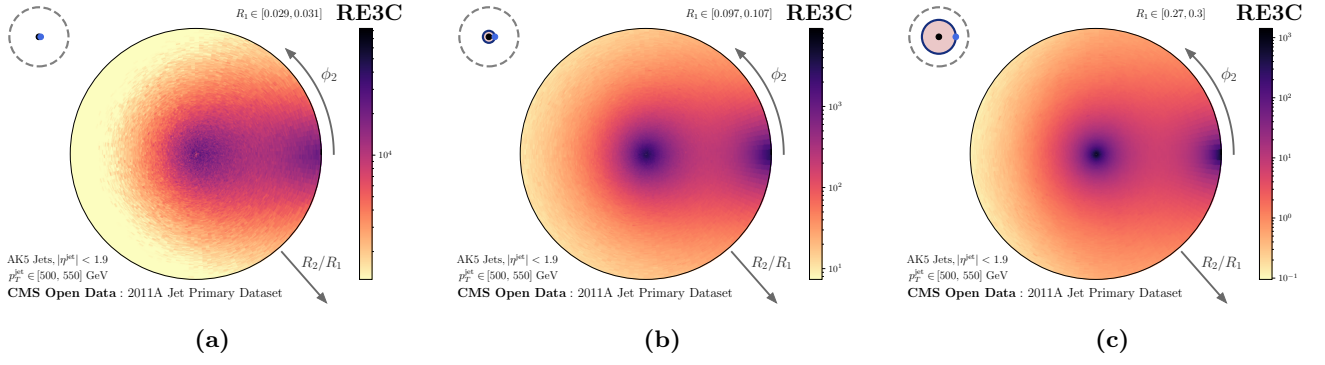


FIG. 3. Additional polar heat maps for RE3Cs evaluated on CMS Open Data. There are enhanced correlations when $R_2 \sim 0$, corresponding to the collinear enhancement as i_2 approaches s , and when $\phi_2 \sim 0$, $R_2 \sim R_1$, corresponding to $i_2 \rightarrow i_1$. The R_1 bin for each plot is indicated by the radius of the filled circle in the top-left inset of each plot.

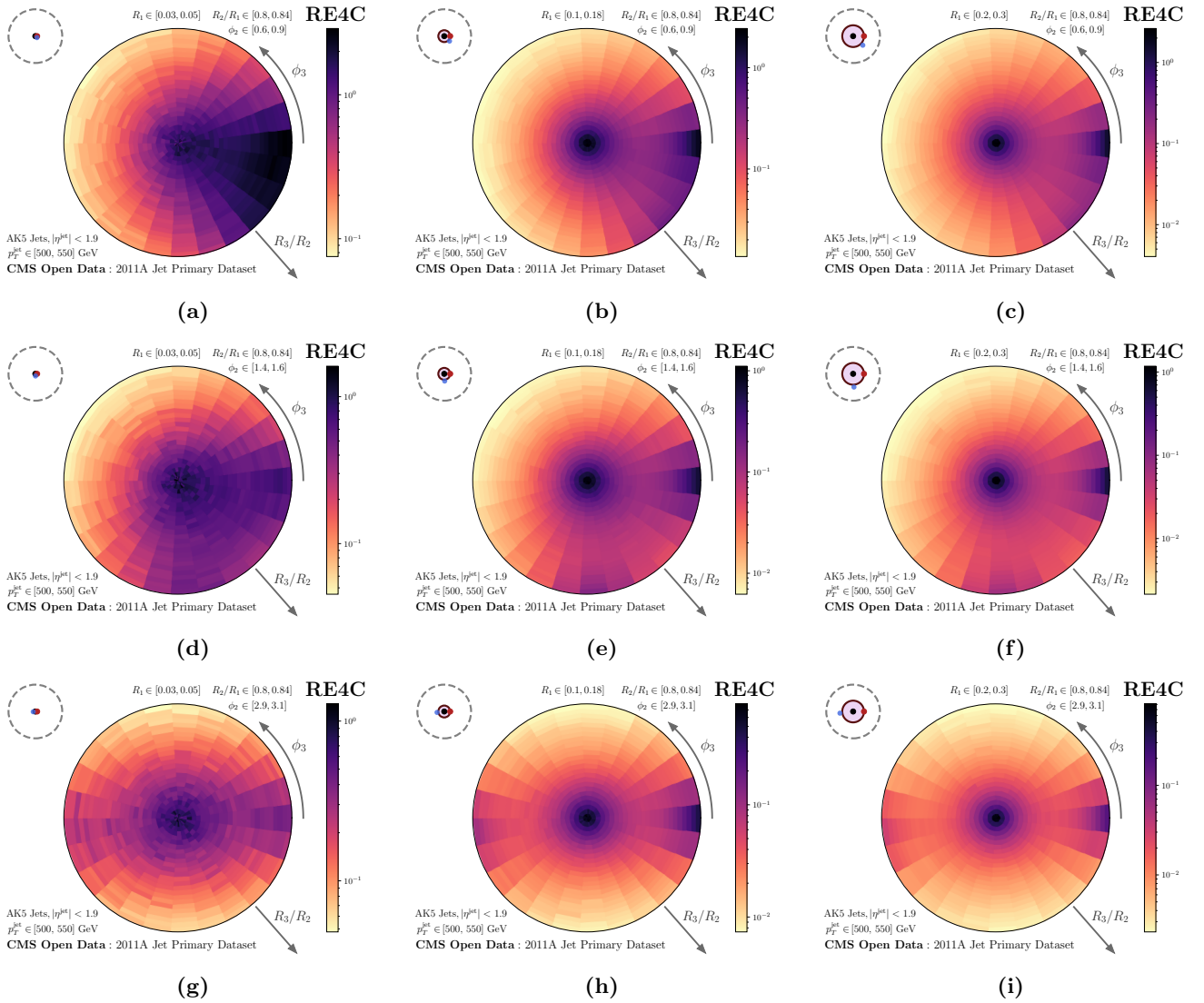


FIG. 4. Polar heat maps for RE4Cs evaluated on CMS Open Data, with ϕ_2 centered near 45° (top row), 90° (middle row) and 180° (bottom row). We highlight that, relative to the RE3C presented in Fig. 3, there are enhanced correlations when $\phi_3 \sim -\phi_2$, corresponding to the collinear enhancement of radiation as i_3 approaches i_1 .

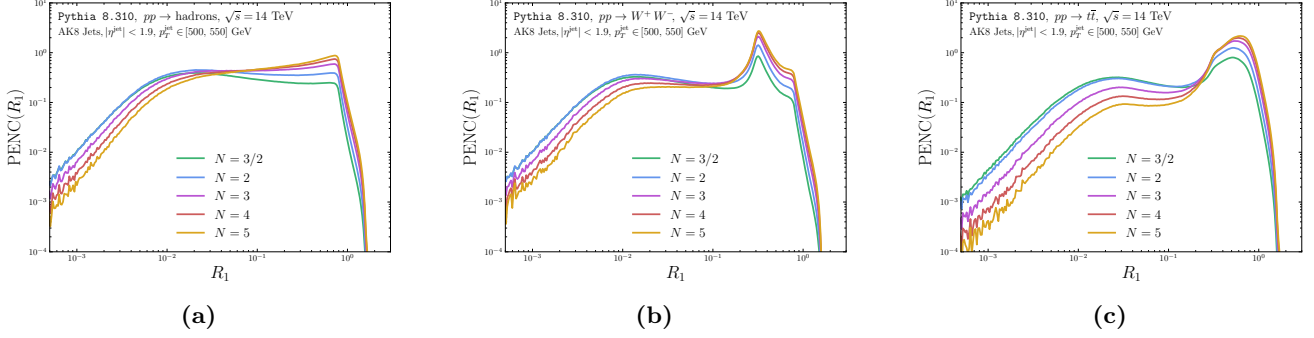


FIG. 5. PENCs for (a) QCD-, (b) W - and (c) top-quark-initiated jet samples generated with `Pythia 8.310`. Jets are clustered using the anti- k_t algorithm with a radius parameter of $R = 0.8$, and have transverse momenta in the range $p_T^{\text{jet}} \in [500, 550]$ GeV and pseudo-rapidities in the range $|\eta^{\text{jet}}| < 1.9$. PENCs for W - and top-quark-initiated jets feature enhanced correlations at scales correlated with the W -boson and top-quark masses.

Appendix D: Process Dependence: Pythia Samples

This appendix provides visualizations for energy correlators evaluated on Monte Carlo samples of QCD-, W -, and top-initiated jets generated in `Pythia 8.310`, as detailed in Table I, which emphasize both the broad range of applications and the visually intuitive representations of jet substructure that are achieved by our new parametrization for RE3Cs. We begin by showing PENCs evaluated on each jet sample in Fig. 5, which provide simple, albeit less fetching, visualizations which clearly distinguish each sample of jets.

The visually distinct features of each jet sample are even more evident as more particles are resolved, i.e. by the RE3C and RE4C. In Fig. 6, we present bullseye visualizations of the RE3C for each jet sample in several R_1 bins; as in the plots using CMS Open Data in the previous appendix, the radial variable and polar angle for each RE3C bullseye are the ratio R_2/R_1 and the angle ϕ_2 , respectively. We note that the rings in the polar heat maps for the RE3C are correlated with the mass of the W boson, in that they appear at the angular scale $R_2 \simeq 0.3 \sim 2m_W/p_T^{\text{jet}}$.

The bullseye of representation of the RE3C we introduce are similar to the analogous bullseye representations of the traditional E3C for each jet sample, shown in Fig. 7, for which the radial variable is the ratio R_S/R_L and the polar angle is the associated azimuthal angle. However, the traditional E3C shows only a small slice of the information of the RE3C we introduce in this work, and the RE3C introduced in this work contains additional information about the relative orientations of particles within a jet; for example, Figs. 6(h) and 6(k) can be compared to Figs. 7(h) and 7(k) to conclude that the RE3C we introduce conveys additional information about the orientation of the rings of radiation within W -boson-initiated jets.

Fig. 8 provides similar polar heat maps for R_3/R_2 and ϕ_3 for the RE4C, within several ϕ_2 bins, and for R_2 near R_1 . As in the case of the RE4Cs evaluated on CMS Open Data, we also see prominent correlations when $\phi_3 \sim -\phi_2$ when R_2 is near R_1 , corresponding to the case that particle i_3 approaches particle i_1 . These correlations for $\phi_3 \sim -\phi_2$ quickly diminish as R_2 is decreased and no longer near R_1 .

Finally, we visualize the ϕ_2 -integrated RE3Cs for each jet sample in the first row of Fig. 9 and the R_M -integrated traditional E3Cs in the second row. Much as in the case of the polar heat maps, the integrated RE3Cs densities provide strictly more information than the densities associated with traditional E3Cs. These provide a clear visual distinction between each sample of jets.

Appendix E: Non-Perturbative Features

Finally, we investigate the non-perturbative features of the new RENCs we introduce in this work, focusing on the example provided by the density plots for the ϕ_2 -integrated RE3C which we visualize again in Fig. 10. For notational convenience in the discussion below, we let p_T be shorthand for p_T^{jet} . Unlike in the traditional E3C, for which there are only non-perturbative effects in the squeezed configuration with $R_S \sim \Lambda_{\text{QCD}}/p_T$, our new RE3C exhibits non-perturbative features in two regimes: (1) when $R_2 \sim \Lambda_{\text{QCD}}/p_T$, when particle i_2 (the emission that sets R_2) approaches the special particle s ; and (2) when $R_1 - R_2 \sim \Lambda_{\text{QCD}}/p_T$, with the possibility that i_2 approaches i_1 .

However, the shapes of the non-perturbative features of the integrated RE3C of Fig. 10(a) are not exactly symmetric under a reflection about the line $R_2 = R_1/2$: the ridge in Fig. 10(a) when $R_2 \rightarrow R_1$ has a smaller slope than the ridge

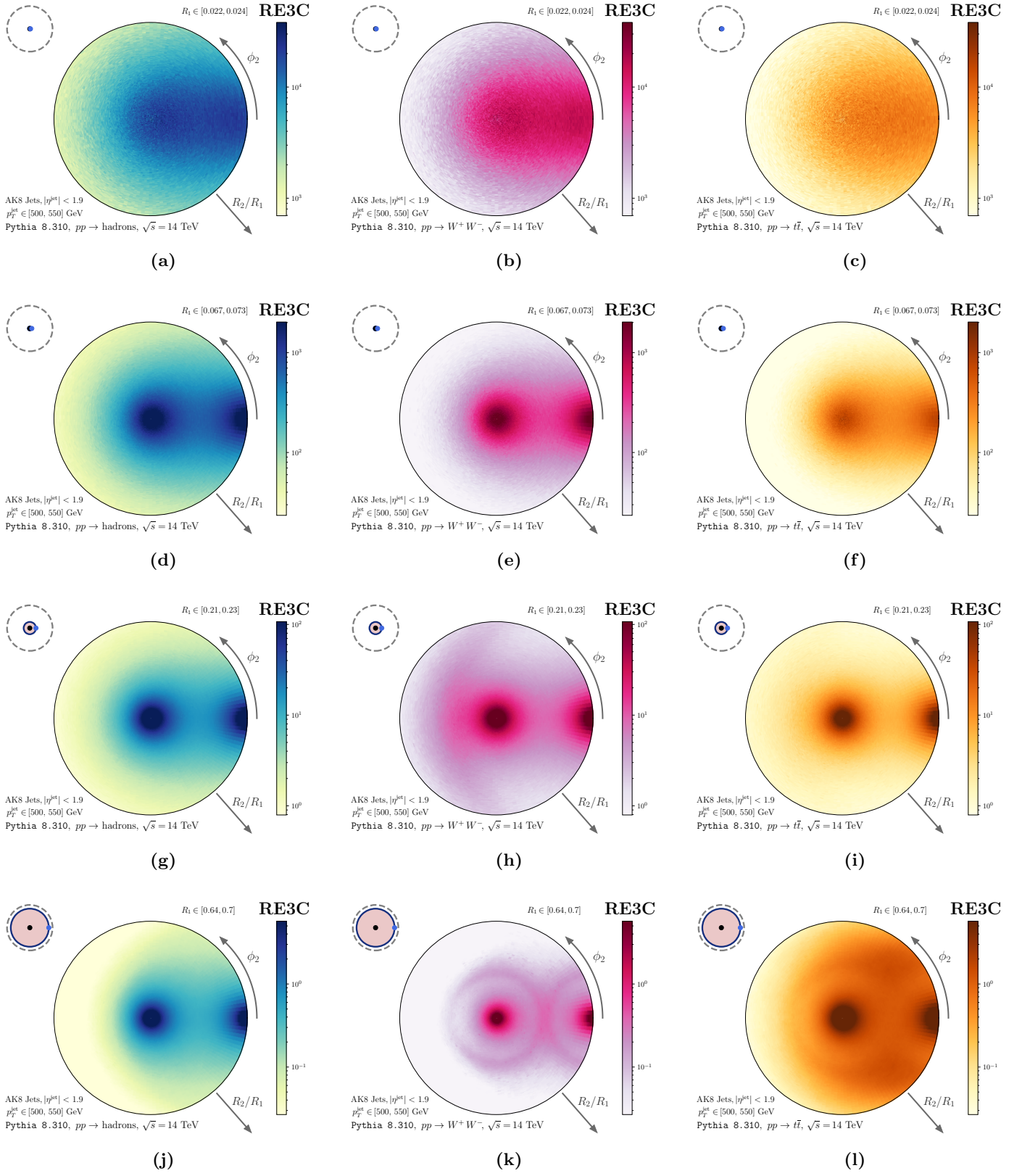


FIG. 6. Polar heat maps of the RE3C we introduce in this work for (first column) QCD-, (second column) W^- , and (third column) top-quark-initiated jets. The radial direction in each plot is the ratio R_1/R_2 , and the polar angle of each plot indicates the angle ϕ_2 . Our RE3Cs provide a clear visual representation of the distinct patterns of radiation in each jet sample at different scales (set by R_1).

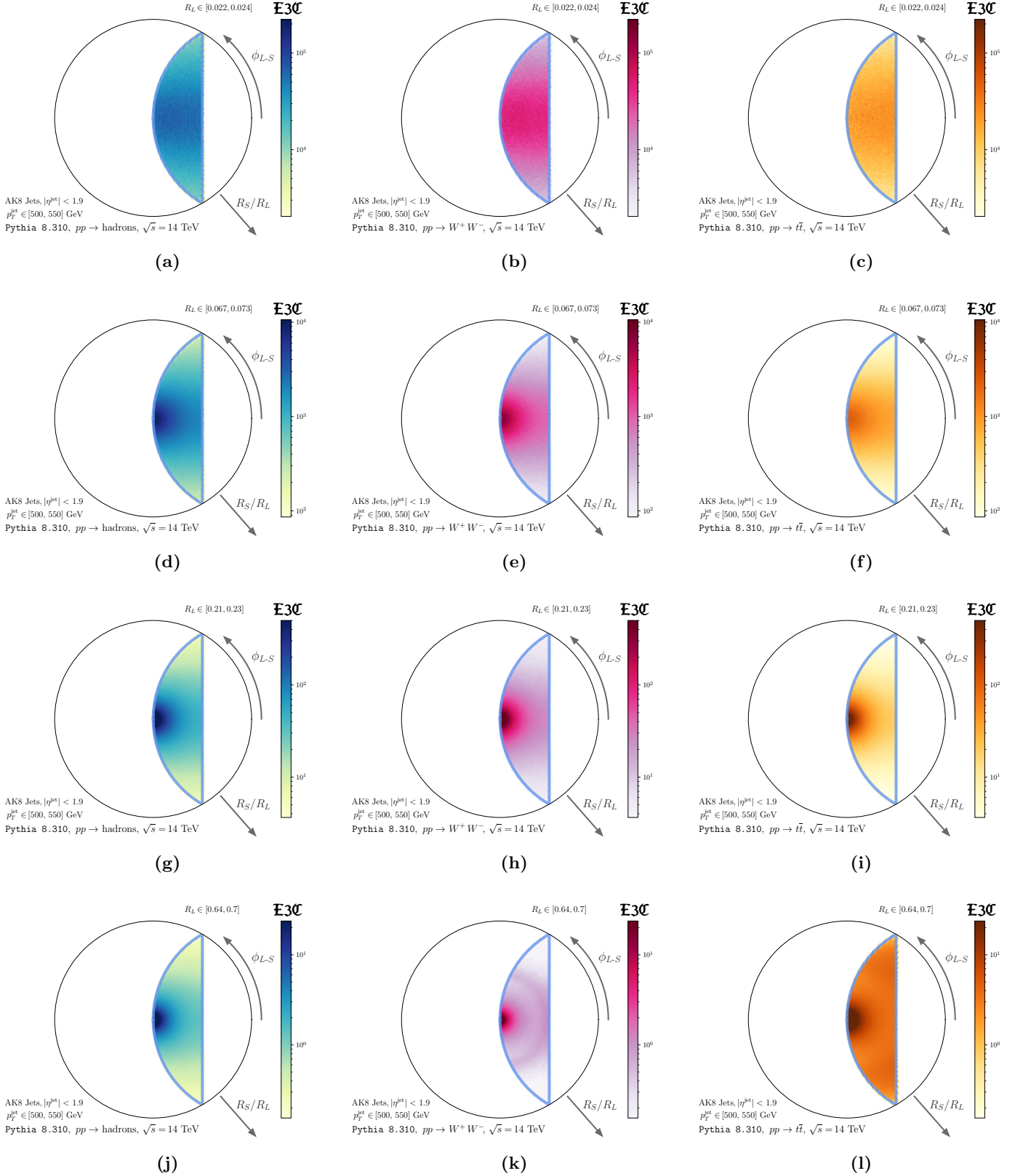


FIG. 7. Polar heat maps of the traditional E3C for (first column) QCD-, (second column) W^- , and (third column) top-quark-initiated jets. The radial direction in each plot is the ratio R_S/R_L , and the polar angle of the plot corresponds to the angle between the lines whose lengths determine R_S and R_L . The R_L bins for each plot are chosen to be the same as the R_1 bins in Fig. 6. The polar heat maps of the traditional E3C contain similar information as the RE3Cs introduced in this work and shown in Fig. 6; however, the traditional E3C does not capture all the orientation information about radiation patterns in each jet sample that is present in our new RE3C.

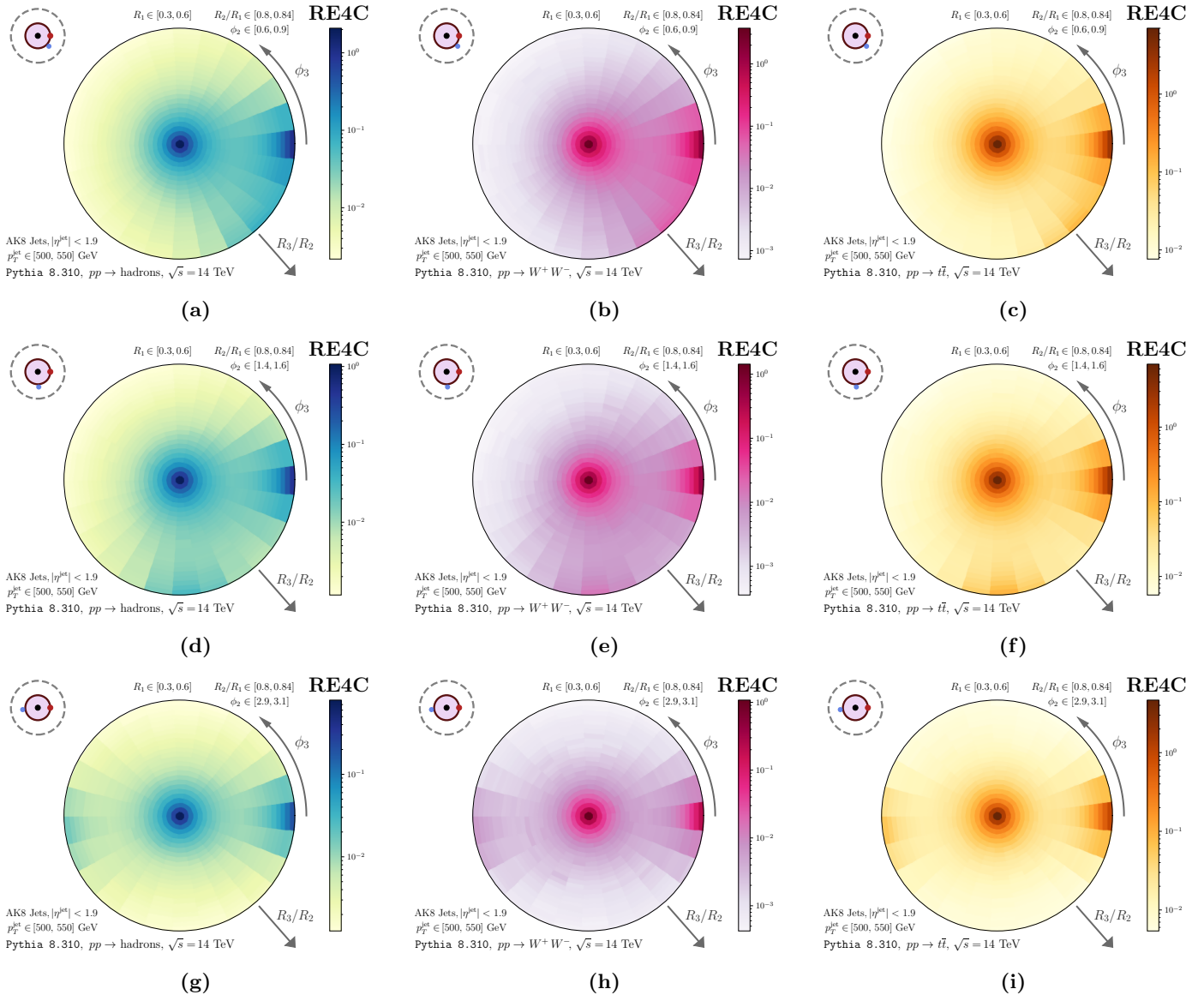


FIG. 8. Bullseye visualizations of the RE4C evaluated on QCD-, W^- , and top-quark-initiated jets generated with Pythia 8.310, in the style of Fig. 4. As in Fig. 4, there are also enhanced correlations in energy when ϕ_3 is near $-\phi_2$.

when $R_2 \rightarrow 0$. Concretely, this means that R_2 must get closer to R_1 in order for non-perturbative features to emerge than we might naively expect. We refer to this as the “ R_2 -asymmetry” of the integrated RE3C.

To explain this R_2 -asymmetry, we note that when $R_2 \sim \Lambda_{\text{QCD}}/p_T$, shown by the dashed yellow line in Fig. 10, the particle i_2 is non-perturbatively close to s , independent of the orientation ϕ_2 of particle i_2 around s . On the other hand, when $R_2 \sim R_1 - \Lambda_{\text{QCD}}/p_T$, particle i_2 is not guaranteed to be near i_1 . Instead, i_2 is only non-perturbatively close to i_1 in a narrow range of azimuthal angles around $\phi_2 = 0$, as visualized in Fig. 10(b). Therefore, it is only when R_2 gets significantly closer to R_1 that the non-perturbative features of the integrated RE3C begin to emerge.

We estimate the R_2 -asymmetry of the integrated RE3C by noting that non-perturbative features emerge when the measure of the non-perturbative phase space for i_2 near i_1 is comparable to the non-perturbative phase space for i_2 near s . This is visualized in Fig. 10(b): non-perturbative features of the integrated RE3C emerge when the length of the green dashed line near i_1 has a length of order Λ_{QCD}/p_T . The associated geometric constraint is a complicated solution to a cubic equation and we do not show it here. However, we show our resulting estimate of the non-perturbative features as the green dashed line in Fig. 10(a), which aligns closely with the non-perturbative ridge of the integrated RE3C as R_2 approaches R_1 .

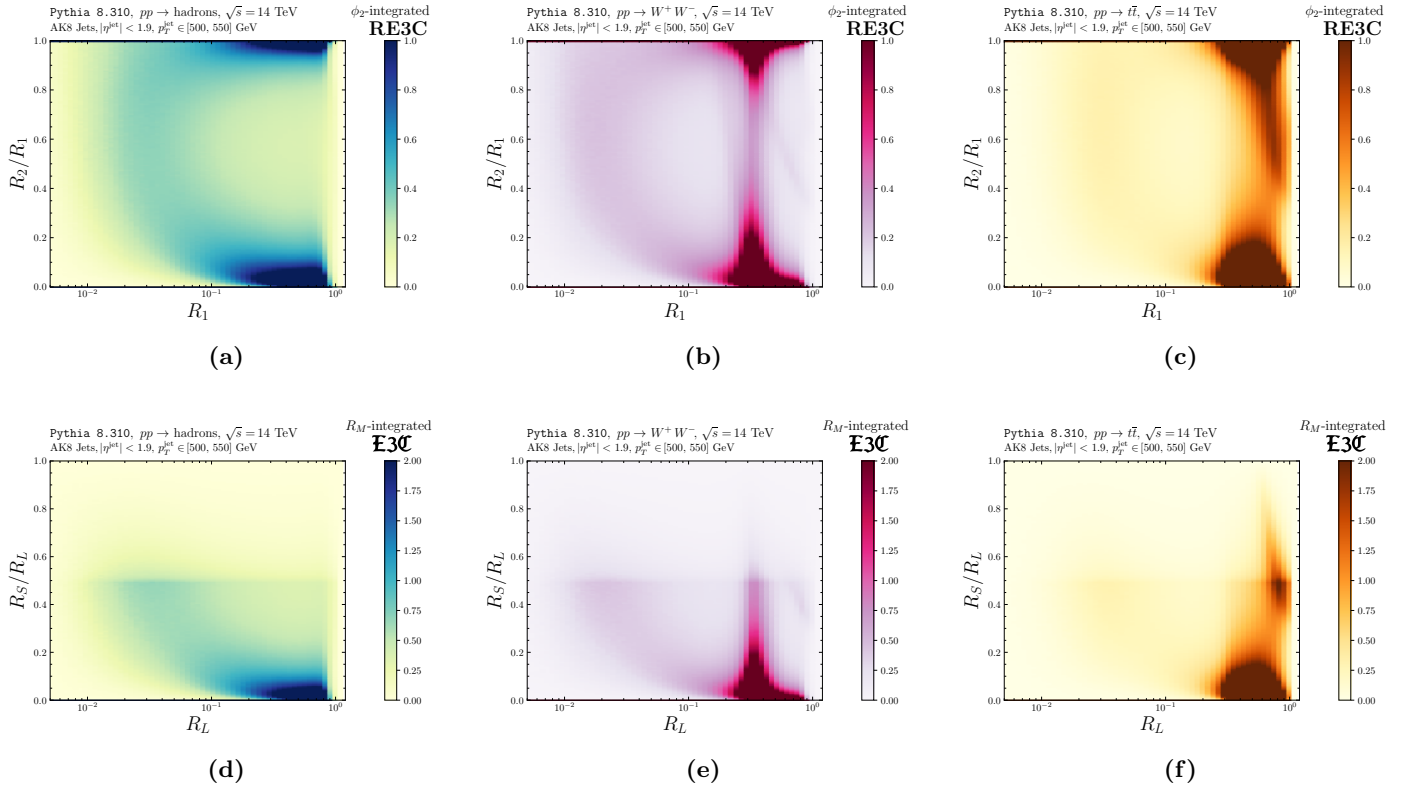


FIG. 9. Density plots for ϕ_2 -integrated RE3Cs (first row) and the analogous R_M -integrated traditional E3Cs (second row), in the style of Fig. 4 of the main text, evaluated on simulated events in `Pythia 8.310`. The first column shows ϕ_2 -integrated RE3Cs for $pp \rightarrow \text{hadrons}$, the second column for $pp \rightarrow W^+W^-$, and the third column for $pp \rightarrow t\bar{t}$. Each row illuminates how three-point energy correlators encode the unique features of each type of jet. We note that the information of the traditional E3C is a subset of the information conveyed by the RE3C we introduce in this work.

-
- [1] Lance J. Dixon, Ian Moulton, and Hua Xing Zhu, “Collinear limit of the energy-energy correlator,” *Phys. Rev. D* **100**, 014009 (2019), arXiv:1905.01310 [hep-ph].
 - [2] Hao Chen, Ian Moulton, XiaoYuan Zhang, and Hua Xing Zhu, “Rethinking jets with energy correlators: Tracks, resummation, and analytic continuation,” *Phys. Rev. D* **102**, 054012 (2020), arXiv:2004.11381 [hep-ph].
 - [3] Jasmine Brewer, José Guilherme Milhano, and Jesse Thaler, “Sorting out quenched jets,” *Phys. Rev. Lett.* **122**, 222301 (2019), arXiv:1812.05111 [hep-ph].
 - [4] “CERN Open Data Portal,” <http://opendata.cern.ch>.
 - [5] CMS Collaboration, “Jet primary dataset in AOD format from RunA of 2011 (/Jet/Run2011A-12Oct2013-v1/AOD),” CERN Open Data Portal (2016), 10.7483/OPENDATA.CMS.UP77.P6PQ.
 - [6] Patrick T. Komiske, Radha Mastandrea, Eric M. Metodiev, Preksha Naik, and Jesse Thaler, “Exploring the Space of Jets with CMS Open Data,” *Phys. Rev. D* **101**, 034009 (2019), arXiv:1908.08542 [hep-ph].
 - [7] Patrick Komiske, Radha Mastandrea, Eric Metodiev, Preksha Naik, and Jesse Thaler, “CMS 2011A Open Data || Jet Primary Dataset || pT > 375 GeV || MOD HDF5 Format,” (2019), 10.5281/zenodo.3340205.
 - [8] Christian Bierlich *et al.*, “A comprehensive guide to the physics and usage of PYTHIA 8.3,” *SciPost Phys. Codeb.* **2022**, 8 (2022), arXiv:2203.11601 [hep-ph].
 - [9] Peter Skands, Stefano Carrazza, and Juan Rojo, “Tuning PYTHIA 8.1: the Monash 2013 Tune,” *Eur. Phys. J. C* **74**, 3024 (2014), arXiv:1404.5630 [hep-ph].
 - [10] Matteo Cacciari, Gavin P. Salam, and Gregory Soyez, “The anti- k_t jet clustering algorithm,” *JHEP* **04**, 063 (2008), arXiv:0802.1189 [hep-ph].
 - [11] Patrick T. Komiske, “EnergyEnergyCorrelators package,” <https://github.com/pkomiske/EnergyEnergyCorrelators>.
 - [12] Samuel Alipour-fard, “ResolvedEnergyCorrelators (RENCs),” <https://github.com/samcaf/ResolvedEnergyCorrelators> (2024).

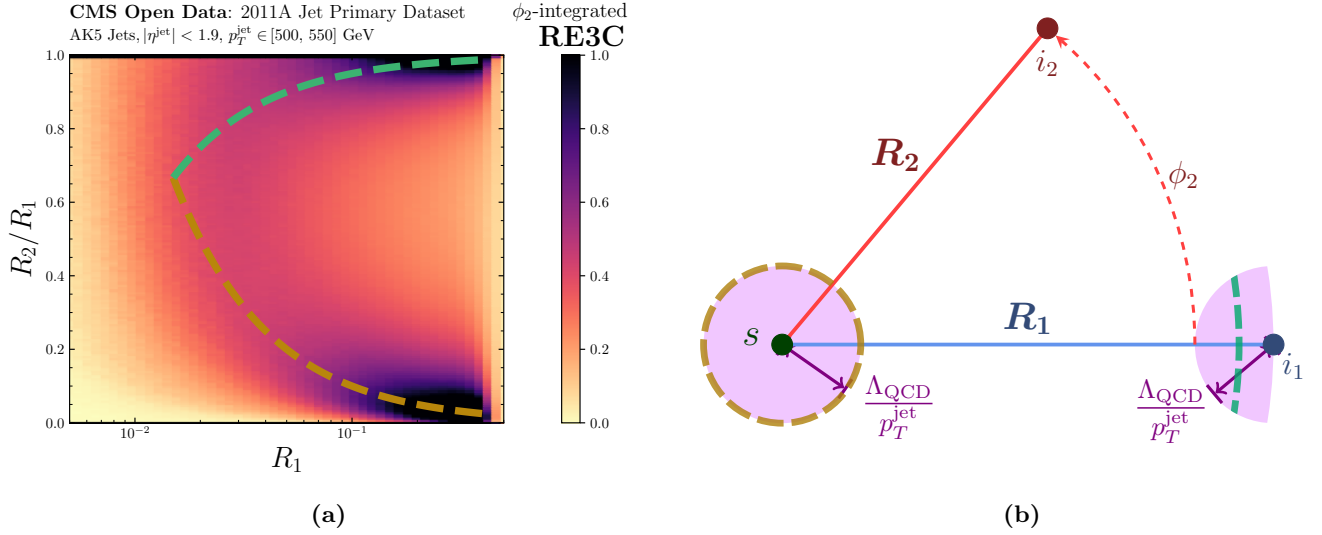


FIG. 10. Depictions of the non-perturbative features of the RE3C introduced in this work **(a)** highlighted in a two-dimensional density plot, and **(b)** in a simple cartoon demonstrating the relevant non-perturbative regimes. **(a)** A density plot for the RE3C evaluated on CMS Open Data and integrated over ϕ_2 , taken from Fig. 4 of the main text, together with dashed lines indicating where non-perturbative effects are expected to become important using (geometric) phase space considerations. **(b)** The RE3C geometry, with non-perturbative regions of phase space highlighted in purple, and with the dashed lines near s and i_2 indicating the values of R_2 where we expect non-perturbative features to emerge in the integrated RE3C.